

Vertical Pyro-Phototronic Effect and Lateral Photothermoelectric Effect in Perovskite Single Crystals-Based Photodetector for Narrowband and Broadband Dual-Modal Optical Communications

Wenzhi Hu, Rui Yan, Yunxia Ma, Ridong Cong, Xingkun Ning, Dan Zhang, Yao Liu, Leipeng Li, Shufang Wang, Zheng Yang,* Caofeng Pan,* and Linjuan Guo*

Creating dual-modal metal halide perovskite (MHP)-based photodetectors (PDs) capable of working in either broadband or narrowband modes would enhance optical communication systems. However, challenges such as complex fabrication, and limited detection range (<900 nm) still exist. Herein, self-powered, dual-modal PDs-based on MHPs are demonstrated, which integrate vertical interfacial pyro-phototronic effect (IPPE) and lateral photothermoelectric effect (PTEE), via doping these crystals with Ag⁺ and integrating with wide spectrum absorber. The high-performance narrowband photodetection results from vertical charge collection narrowing effect (CCN)-assisted IPPE, enabling light with specific wavelength to penetrate into the interface, with high carrier separation efficiency and temperature rise. In lateral PD, broadband metamaterial absorbers as counter electrodes improved photothermal conversion and expanded light absorption, achieving ultra-broadband responses from 360 to 2200 nm. By changing the halide type of the MHP single crystals (SCs), the specific response band of narrowband PD can be modulated from purple light to red light, while maintaining the wide spectrum response capability. The dual-modal photodetection is fully used to achieve double encryption during signal transmission. The work offers a promising approach for designing multi-modal PDs for wireless communication and data security, applicable in optical imaging, biomedical, and intelligent sensing.

environmental monitoring, and industrial production.^[1–4] Secure optical communication has gained significant interest due to the risks of information leakage during open light transmission.^[5–6] In these systems, the photodetector (PD), which converts optical signals to electrical ones, is crucial for the speed, accuracy, and security of data transmission.^[7–9] However, traditional PDs typically perform either broadband or narrowband detection.^[10–13] Broadband PDs cover a wide spectral range from ultraviolet (UV), visible, and near-infrared (NIR) to terahertz and are easy to produce due to the wide optical absorption of photoactive materials. In contrast, narrowband PDs are limited to specific spectral ranges. Single-modal PDs are inadequate for optical communication encryption because they require separate devices for different signal bands. Developing a dual-modal photodetection method that can handle both broadband and narrowband signals is crucial.^[7,8,14] However, integrating dual-modal PDs into a single device is challenging due to complexities in material and structural design.^[5,15]

1. Introduction

Optical communication is a high-speed, energy-efficient technology with large capacity, commonly used in remote sensing,

Metal halide perovskites (MHPs) are promising for broadband and narrowband PDs due to their high light absorption, long carrier lifetime, excellent mobility, easy fabrication, and tunable bandgap.^[16–20] However, dual-modal photodetection with MHPs

W. Hu, R. Yan, Y. Ma, R. Cong, X. Ning, D. Zhang, Y. Liu, L. Li, S. Wang, Z. Yang, L. Guo
Hebei Key Laboratory of Photo-Electricity Information and Materials
College of Physics Science and Technology
Hebei University
Baoding 071002, P. R. China
E-mail: yangzheng06@hbu.edu.cn; guolinjuan@hbu.edu.cn

L. Li, Z. Yang
Institute of Life Science and Green Development
Hebei University
Baoding 071002, P. R. China
C. Pan
Institute of Atomic Manufacturing
Beihang University
Beijing 100191, P. R. China
E-mail: pancaofeng@buaa.edu.cn

 The ORCID identification number(s) for the author(s) of this article can be found under <https://doi.org/10.1002/lpor.202401990>

DOI: 10.1002/lpor.202401990

has seen limited progress. Li's group achieved narrowband and broadband dual-modal detection in one device without bias by using polyvinylpyrrolidone and methylamine gas to vary the perovskite film thickness in different areas.^[7] Lei's team created a dual-modal PD using MAPbI_{3-x}Br_x/n-MAPbBr₃/MAPbI₃ perovskite single crystals, which adjusts photon absorption and carrier transport through voltage bias.^[21] They also developed a perovskite single-crystal heterojunction dual-band PD that detects UV broadband and NIR narrowband light, utilizing a discontinuous electric field in a vertically stacked structure.^[8] Investigations of dual-modal MHP-based PDs face challenges like fabrication complexity, lattice and thermal mismatches, and a limited detection range due to bandgap constraints (< 900 nm). Therefore, there is a need for dual-band PDs in a single device that can detect a wider range (up to 2200 nm), feature a simpler design, and offer improved performance at zero bias.

Thermal detectors are recognized for their wide spectral response from UV to terahertz at room temperature. They operate by measuring temperature-dependent properties, such as resistance in bolometers, voltage in photothermoelectric (PTE) detectors, and spontaneous polarization in pyroelectric (PE) detectors. The PTE PDs enable a broad photoresponse, with no requirement of bias voltage or chopper.^[22] MHPs show promise as thermoelectric materials due to their low thermal conductivity, good mobility, and adjustable charge carrier properties. Some perovskites have been used for infrared PTE detection beyond their bandgap.^[23-24] However, low electrical conductivity limits their progress as PTE materials, necessitating effective solutions.^[25-26] To tackle this issue, effective strategies such as doping^[27-30] are crucial. Moreover, achieving narrowband spectral detection requires pairing PTEE-based PDs with bandpass filters, complicating the device structure. The charge collection narrowing (CCN) effect is a well-established method for narrowband photodetection using MHPs,^[31-33] is due to strong surface-charge recombination of excess carriers near crystal surfaces caused by short-wavelength light. Additionally, the interfacial pyro-phototronic effect (IPPE) has been effectively used to improve self-powered PDs-based on heterojunctions or Schottky junctions.^[10,34] IPPE results from changes in interfacial polarization intensity due to band bending at the junction, influenced by the cooling of photogenerated charge carriers^[35-37] and the resulting temperature increase. Combining CCN and IPPE enables high-performance, self-powered narrowband photodetection. Therefore, utilizing the interaction between the vertical CCN-IPPE and lateral PTEE in MHP-based heterojunctions could be promising to construct high-performance broadband and narrowband dual-modal PDs. Given the challenges, it's essential to create a straightforward strategy for producing vertical IPPE and lateral PTEE-based MHP PDs integrated in one device for dual-modal optical communications.

Herein, we present self-powered narrowband and broadband dual-modal PDs using MAPbX₃ (MA = CH₃NH₃⁺, X = Cl⁻, Br⁻, and I⁻) single crystals (SCs), integrating vertical IPPE and lateral PTEE. Coating the SCs with AgBr forms a highly conductive n-doping layer,^[38] simultaneously serving as a thermoelectric layer and creating a p-n junction (MAPbX₃/MAPbX₃:Ag⁺) with the intrinsic perovskites. The high-performance narrowband photodetection is due to the vertical CCN-assisted IPPE, which allows light near the bandgap to penetrate the interface, maximizing car-

rier separation efficiency and causing temperature increases. For instance, the MAPbBr₃/MAPbBr₃:Ag⁺ p-n junction achieved a peak current responsivity (*R_i*) of 0.36 A W⁻¹ and a response time of 77 μs under 532 nm light. In lateral PD, broadband metamaterial absorbers were used as counter electrodes on the MAPbX₃:Ag⁺ layer, enhancing photothermal conversion efficiency and expanding light absorption range resulted in ultra-broadband responses from 360 to 2200 nm, achieving a voltage responsivity (*R_v*) of 0.49 V W⁻¹ at 2200 nm. By utilizing dual-modal photoreponses to UV, visible, and NIR light in MAPbBr₃/MAPbBr₃:Ag⁺ p-n junction-based PDs, a secured optical communication system was conceptually demonstrated for both frontal and reverse incidence. Our work offers a promising approach to designing multi-modal PDs for wireless communication and data security, applicable in optical imaging, biomedical, and intelligent sensing.

2. Results and Discussion

Three typical MHP single crystals (MAPbCl₃, MAPbBr₃, and MAPbI₃) were grown using typical inverse temperature crystallization. PTFE molds of varying depths were used to produce SCs with thicknesses of 0.5-3 mm. To prevent residual liquids from causing rough surfaces and defects during extraction, the SCs were polished with abrasive papers to improve contact with electrodes prior to further characterizations and device fabrications. The Experimental Section thoroughly describes the methods used to grow the SCs. Figure S1a,d, and g (Supporting Information) show photos of MAPbCl₃, MAPbBr₃, and MAPbI₃ SCs, all with uniform, defect-free morphology. The crystal structures of MAPbCl₃, MAPbBr₃, and MAPbI₃ SCs were confirmed using X-ray diffraction (XRD) spectra. The XRD pattern for MAPbCl₃ SC shows (001), (002), and (003) peaks at 2θ values of 15.84°, 31.69°, and 48.2°, respectively, as seen in Figure S1b (Supporting Information). Similarly, MAPbBr₃ SC displays peaks at 15.12°, 30.3°, and 46.03°, as shown in Figure S1e (Supporting Information). Figure S1h (Supporting Information) shows the XRD pattern of the MAPbI₃ single crystal SC, displaying only the (200) and (400) sharp peaks at 2θ values of 20.02° and 40.41°, confirming its single-crystalline nature with exposed (100) faces. All the results indicate the successful growth of high-quality MAPbX₃ SCs. The absorption spectra in Figure S1c,f, and i (Supporting Information) reveal bandgaps of 2.87 eV for MAPbCl₃ SC, 2.15 eV for MAPbBr₃ SC, and 1.474 eV for MAPbI₃ SC. Photoluminescence spectra show peaks at around 404 nm, 531 nm, and 781 nm, respectively. Ultraviolet photoelectron spectroscopy (UPS) spectra, shown in Figure S2 (Supporting Information), were used to determine the energy band structures of MAPbCl₃, MAPbBr₃, and MAPbI₃ SCs-based on UPS and absorption spectra data, energy band diagrams for three SCs reveal weak p-type conductivity. The low conductivity of MHP SCs limits high-performance PTE device development. To enhance conductivity, Ag⁺ doping was applied, transforming the MHP SCs from intrinsic to highly conductive. This was achieved by thermally evaporating a thin layer of AgBr onto the crystal surface and annealing at 85 °C for 15 min. Figure 1a shows that X-ray photoelectron spectroscopy (XPS) confirmed the successful doping of silver ions on the surface of MAPbBr₃:Ag⁺ after annealing. To optimize thermal evaporation

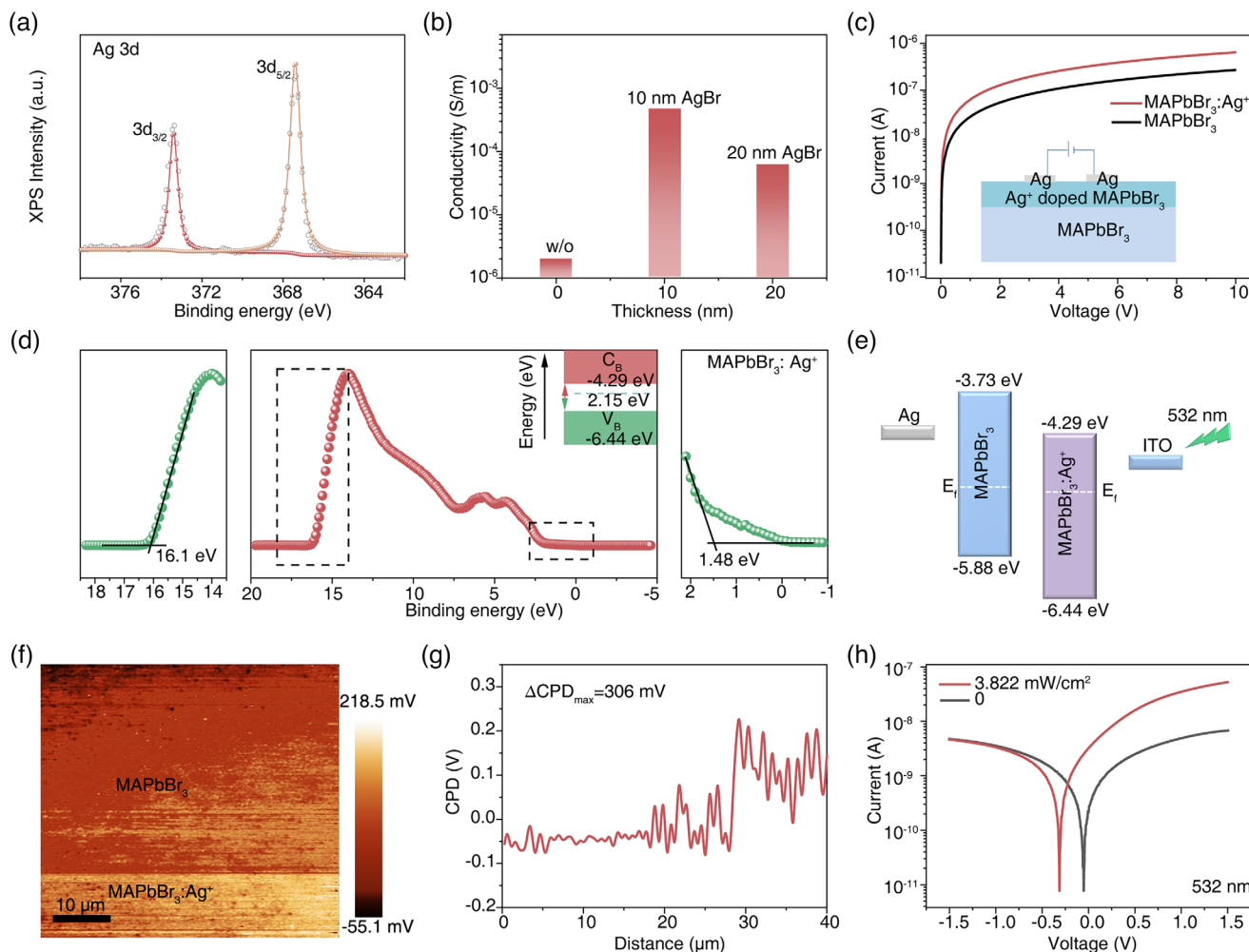


Figure 1. Surface doping of MAPbBr₃ SC by Ag⁺. a) XPS scans of the Ag 3d measured from the Ag⁺ doped MAPbBr₃ surface. b) Electrical conductivity of SC⁺ surface before and after evaporation of AgBr with different thicknesses. c) Dark I-V characteristics of lateral structure devices-based on MAPbBr₃ SC without and with Ag⁺ doping. d) UPS of the surface of MAPbBr₃: Ag⁺ SC. The inset is the corresponding energy band diagram with the green dotted line as the fermi level. e) Energy band diagram of the vertical p-n junction formed between intrinsic p-type MAPbBr₃ bulk and n-type MAPbBr₃: Ag⁺ layer (MAPbBr₃/MAPbBr₃: Ag⁺). f) CPD image and cross-sectional curve g) of Ag⁺ doped treated MAPbBr₃ SC⁺ surface by KPFM measurement. h) The I-V characteristics of vertical MAPbBr₃/MAPbBr₃: Ag⁺ p-n junction under dark and 532 nm laser illumination.

parameters, AgBr films of varying thicknesses were deposited on MAPbBr₃ SCs and annealed. Additionally, four-probes measurements with Ag electrodes were used on lateral structure devices to minimize contact resistance effects on the total current. Figure 1b demonstrates that doping significantly improves the conductivity of the single crystal surface, with a 10 nm AgBr layer being optimal. Consequently, further device fabrication utilized this thickness. The dark currents in MAPbBr₃ lateral devices with a 0.1 mm channel length increased post-AgBr treatment compared to the control device (Figure 1c). Thus, Ag⁺-doped, highly conductive MHP layers are advantageous for PTE device fabrication. Figure 1d, Figure S3a,b (Supporting Information) show the surface UPS of MAPbBr₃, MAPbCl₃, and MAPbI₃ single crystals after Ag⁺ doping, revealing a shift from p-type to n-type, thus forming a vertical p-n junction beneficial for IPPE-based devices (Figure 1e). The work function change in MAPbBr₃ due to Ag⁺ doping was assessed using Kelvin probe

force microscopy (KPFM), covering both doped and undoped regions to observe variations. Figure 1f shows a distinct boundary with a significant contact potential difference (CPD) between the pristine MAPbBr₃ crystal and the Ag⁺-treated area. The CPD, defined as $(\Phi_{\text{tip}} - \Phi_{\text{sample}})/e$, is higher across this boundary (≈ 206 mV) compared to the pristine MAPbBr₃ surface, indicating Ag⁺ n-doping. Additionally, we investigated how annealing duration affects the lateral diffusion of Ag⁺ by comparing two different annealing times (15 and 25 min) after AgBr evaporation on the single crystal surface. KPFM measurement revealed the CPD distribution across the surface of MAPbBr₃ single crystals doped with Ag⁺ and annealed for 25 min, as shown in Figure S4a (Supporting Information). Analysis of the CPD curves in Fig S4b reveals that increasing the annealing time from 15 to 25 min results in greater silver ion lateral diffusion distances. To examine how annealing duration affects silver ion lateral diffusion, we analyzed EDS images of Ag⁺-doped single crystal surfaces

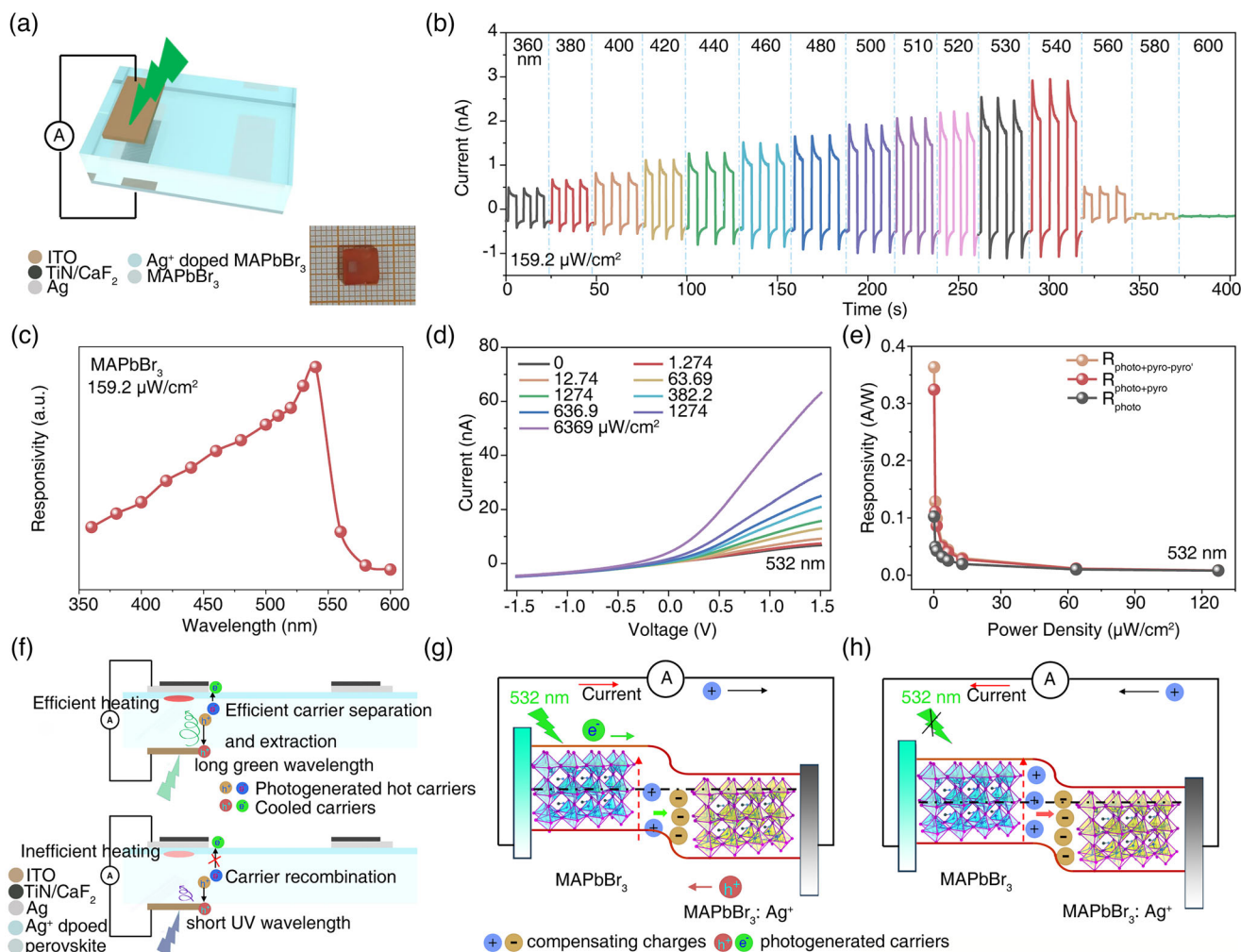


Figure 2. Performances and working mechanism of the vertical narrowband PD-based on MAPbBr₃ SC. a) The schematic diagram of a MAPbBr₃-based vertical narrowband PD. Inset: the photograph of the real device. b) The spectral photoresponses of the PD in the range of 360–600 nm wavelength. c) Normalized R_l of vertical PD in the range of 360–600 nm wavelength. d) I - V characteristics of the vertical PD under dark and 532 nm laser illumination with different power densities. e) The zero bias responsivities of the vertical PD as a function of the power density. f) Working mechanism of narrowband detection using the CCN-assisted IPPE. Schematic energy band diagrams of the MAPbBr₃/MAPbBr₃: Ag⁺ p-n junction-based PD at the beginning of the turning on g) and turning off h) the laser, showing the working mechanism of IPPE.

at annealing times of 15 and 25 min. Analysis of the diffusion regions, as shown in Figures S5a,b (Supporting Information), revealed that the 25-minute annealing treatment resulted in a notably wider diffusion area compared to the 15-minute treatment. These results demonstrate that extended annealing duration promotes enhanced lateral diffusion of Ag⁺. Additionally, I - V measurements of the vertical device under dark and 532 nm laser illumination demonstrate rectification characteristics, which further confirms the formation of p-n junction after Ag⁺ doping. Moreover, the dark capacitance of MAPbBr₃/MAPbBr₃: Ag⁺ p-n junction at zero bias was ≈ 2.23 nF cm⁻². By performing linear fitting of $C(V)^{-2}$ versus the bias voltage (the Mott-Schottky curve), a V_{Bi} (built-in potential) of 0.31 V was obtained (inset of Figure S6, Supporting Information), furthering proving the existence of the p-n junction, which is the basis of the interfacial polarization.

Based on the p-n junctions formed by Ag⁺ doping, we first fabricated three kinds of vertical narrowband PDs-based on

MAPbX₃/MAPbX₃: Ag⁺ (X = Cl, Br, I) p-n junctions. To leverage the responsivities (R) and the narrowband characteristics, the thicknesses were optimized to be 0.8 mm, 1 mm, and 1.5 mm for MAPbCl₃, MAPbBr₃, and MAPbI₃ SCs, respectively, according to the photoelectric performance tests. Figure 2a illustrates the schematic diagram of a MAPbBr₃-based vertical narrowband PD with the inset showing the photograph of the real device. The light shines from the bottom side onto the ITO electrode. The top electrode is the Ag electrode. Then, the narrowband response nature of our optimum MAPbBr₃-based vertical PD was further analyzed by measuring its on-off photoresponses under zero bias over a wide range of wavelengths ranging from 360 to 600 nm with a constant power density of $159.2 \mu\text{W cm}^{-2}$, using a mercury lamp equipped with a monochromator. The photoresponses exhibit a typical four-stage behavior with distinct positive and negative pyroelectric peaks due to the IPPE. As shown in Figure S7 (Supporting Information), four currents $I_{\text{pyro+photo}}$,

I_{photo} , I_{pyro} , and $I_{\text{pyro+photo}} - I_{\text{pyro}}$ can be found in one cycle of on-off photoresponse. The difference between the dark current baseline and the photocurrent plateau represents the magnitude of the I_{photo} . $I_{\text{pyro+photo}}$ represents the difference between the positive pyroelectric spike and the dark current platform. I_{pyro} represents the difference value between the dark current baseline and the negative pyroelectric spike. The difference between the positive and negative pyroelectric peaks is defined as $I_{\text{pyro+photo}} - I_{\text{pyro}}$. The output currents increase steadily between 360 and 540 nm but decrease sharply beyond 540 nm. Figure 2c shows the wavelength-dependent R , which displays a narrowband photoresponse with a full width at half maximum (FWHM) of 113 nm. Since the MAPbBr₃-based vertical PD demonstrates the highest R_I for the light around 540 nm (Figure 2b), a 532 nm laser was selected as the main light source. The self-powered performance of the lateral PDs was thoroughly assessed. Figure 2d presents the I - V curves of the lateral PD in both dark conditions and under 532 nm laser light at varying power levels, revealing rectification and photoresponse indicative of a p-n junction. Figure S8a (Supporting Information) displays the on-off photoresponses of the MAPbBr₃-based vertical PD at 0 V bias under 532 nm light with power densities from 0.127 to 127.4 $\mu\text{W cm}^{-2}$, all showing clear transient pyroelectric responses. As shown in Figure S8b (Supporting Information), all the peak-to-peak current ($I_{\text{pyro+photo}} - I_{\text{pyro}}$), the positive current peak ($I_{\text{pyro+photo}}$), and photocurrent (I_{photo}) monotonously increase with the increase of power density. The self-powered performance of the lateral PDs was thoroughly assessed. The maximum R_I and D^* are 0.36 A W^{-1} and 1.04×10^{14} Jones at the lowest power density of 0.127 $\mu\text{W cm}^{-2}$, respectively (Figure 2e; Figure S7c, Supporting Information). The corresponding dark currents and the noise currents are shown in Figure S9 (Supporting Information). The IPPE-attributed vertical PD exhibits fast response times, with a rise time of 77 μs and a fall time of 157 μs (Figure S8d, Supporting Information). Imaging in Figures S8e and S10 (Supporting Information) shows that laser illumination increases the temperature of SCs compared to dark conditions, with the most significant temperature change observed at 532 nm for MAPbBr₃ SC, aligning with the spectral photoresponses in Figure 2b. Specifically, a 532 nm laser at 4 mW raises the temperature of MAPbBr₃ SC by 3.42 °C. Figure 2f illustrates the narrowing mechanism of vertical IPPE-based PDs, which aligns with CCN-assisted IPPE. Light passes through the transparent ITO electrode, is absorbed by the SC, and generates hot carriers. These carriers undergo thermalization before cooling, reaching an equilibrium state, and are then separated by the built-in field for collection by the electrodes. Inelastic scattering causes energy loss to the lattice, increasing the temperature of the SC. The temperature increase reduces interfacial polarization intensity, producing positive pyroelectric currents through the external circuit, resulting in I_{photo} and I_{pyro} . For shorter wavelengths like 360 nm, the high absorption coefficient of MHP SCs limits their penetration through the SCs, generating charge carriers near the ITO electrode. These charges are easily quenched due to significant surface-charge recombination, leading to the weakened photocurrents. Carrier cooling happens away from the p-n junction interface, and the MHP's low thermal conductivity prevents efficient heating there, leading to limited temperature rise and weak pyroelectric currents. These cause reduced R_I for short-wavelength light due to charge

recombination and inefficient heating. However, light with wavelength near the bandgap, like 532 nm, penetrates deeper, allowing better carrier separation and extraction. The top silver electrode can collect more photogenerated carriers when the long-wavelength laser is incident on the bottom ITO electrode. Carrier cooling near the interface efficiently heats and raises the temperature. However, longer wavelengths, limited by the band gap, reduce light absorption, generate fewer carriers, and result in a weak temperature rise, impairing output currents. Thus, incident light wavelength significantly affects temperature rise and carrier extraction efficiency, leading to the narrowband response of the vertical PDs. The highest R_I can be obtained when light with photon energy near the band gap shines on the PD. The IPPE working mechanism is shown using energy band diagrams of the MAPbBr₃/MAPbBr₃: Ag⁺ p-n junction. An interfacial polarization forms due to the built-in electric field from the band bending at the junction.^[39] Upon exposure to light, as depicted in Figure 2g, the absorption of light generates electron-hole pairs which are propelled by the built-in electric field of the p-n junction, resulting in the production of I_{photo} . Meanwhile, the temperature rise induced by carrier cooling will lead a decrease in the interfacial polarization intensity, generating a transient positive pyroelectric current (I_{pyro}). When the light is off, the cooling of SCs increases interfacial electric polarization (Figure 2h). Additionally, a negative pyroelectric current (I_{pyro}) is generated in the external circuit to facilitate charge redistribution. The aforementioned CCN-assisted IPPE-based narrowband mechanism is applicable to other MHP systems. In addition, we compared the uniformity and stability of the performance of devices with different AgBr thickness. Figure S11a (Supporting Information) demonstrates the performance uniformity across AgBr devices of three different thicknesses. Among these, devices with a 10 nm thickness exhibited superior uniformity. Further analysis of these vertical structure AgBr devices included comprehensive stability tests under moisture and thermal conditions, with results presented in Figure S11b,c (Supporting Information), respectively. We found that the humidity stability of vertical devices with AgBr thickness of 5 nm is slightly worse than that of 10 nm and 20 nm. However, for the thermal stability measurements, the vertical device with AgBr thickness of 20 nm has the worst thermal stability, followed by the device with AgBr thickness of 10 nm. The stability can be enhanced through passivation in the future work. We also evaluated the long-term operational stability of the device and its performance in an open environment (25 ± 5 °C, 40 ± 10 RH%). The photoresponse characteristics were evaluated through 240 consecutive cycles under 532 nm laser illumination at 127.4 $\mu\text{W cm}^{-2}$ (Figure S12a, Supporting Information). The device exhibited consistent photocurrent and dark current levels throughout these cycles, indicating robust operational stability. The results shown in Figure S12b (Supporting Information) indicate that the output currents exhibited only a 4% decline from its initial value over a 22-days' period. For vertical p-n junctions based on MAPbCl₃ and MAPbI₃ SCs, similar interfacial pyroelectric photoresponses are observed, as depicted in Figures S13-S20 (Supporting Information). Specifically, Figure S13b,c (Supporting Information) demonstrate that the output currents and resultant R_I of MAPbCl₃-based PD increase with wavelengths exceeding 250 nm, reaching a peak at 390 nm. Beyond this wavelength, the device's R_I decreases sharply. The FWHM of the

wavelength-dependent R_I is 76 nm, indicating narrowband behavior. Figure S13d (Supporting Information) presents the I - V characteristics of the PDs under both dark and illuminated conditions with varying power intensities, demonstrating rectifying behavior. Figure S15 (Supporting Information) demonstrates that MAPbCl₃ SCs experience the highest temperature increase of 1.05 °C at 405 nm with 2 mW laser power, surpassing the increases at 360 nm, 532 nm, and 635 nm. Figure S16 (Supporting Information) highlights the self-powered performance of the MAPbCl₃-based vertical PD for 405 nm, achieving maximum R_I and D^* values of 7.09 mA W⁻¹ and 3.37×10^{11} Jones at 0.1274 μW cm⁻². The rise and fall times are 120 and 410 μs, respectively (Figure S16e, Supporting Information). For the MAPbI₃ SC-based vertical PD, the peak R_I and maximal temperature increase under light occur at 785 nm, with a R_I FWHM of 249.5 nm (Figure S17c, Supporting Information). It achieves a maximum R_I of 15.3 mA W⁻¹ and a detectivity of 6.95×10^{12} Jones (Figure S20c,d, Supporting Information), allowing detection of light as low as 0.1274 μW cm⁻². The PD's rise and fall times are 31.4 μs and 49 μs, respectively (Figure S20e, Supporting Information). These results indicate that CCN-assisted IPPE is a versatile method for realizing self-powered and narrowband photodetection using MHP SCs.

Ag⁺ doping not only facilitates the formation of a vertical p-n junction, which exhibits narrowband photoresponses but also generates a thin layer with high electrical conductivity. Consequently, lateral PDs-based on the PTEE were developed, leveraging the large Seebeck coefficient and low thermal conductivity of MHP SCs.^[25] Nonetheless, the photothermal conversion efficiencies of MHPs across a broad spectral range are significantly constrained by their bandgap, leading to suboptimal performance in the near-infrared (NIR) region. To address this limitation, a wide-spectrum absorber comprising a titanium nitride (TiN) layer^[40] was integrated into the electrodes to increase photothermal conversion efficiency over a wide spectral range to develop a broadband PD-based on the PTEE. We first examine the TiN-based absorber, where commercial colloidal TiN nanoparticles (NPs) are processed with high-energy ball milling, spin-coated onto a thermally evaporated Ag film, and topped with a CaF₂ antireflection layer. XRD patterns in Figure S21a (Supporting Information) confirm the cubic crystal structure of the TiN NPs. The absorber's thickness plays a crucial role in its photothermal conversion efficiency. The broadband detection capability spanning 360–2200 nm observed in this study is primarily attributed to the unique absorption characteristics of the absorber within this spectral range. Previous research has demonstrated that several factors influence the absorption properties of titanium nitride-based absorbers in this wavelength band. Through a systematic analysis of experimental results, several critical parameters have been identified as determinants of the broadband detection range: the composition and properties of the substrate reflective layer, the dimensional precision of the TiN layer, and the characteristics of the top anti-reflection film. Additionally, as illustrated in Figure S21b (Supporting Information), the spin coating rate is identified as a significant parameter influencing the broadband detection capabilities of the device. The absorption intensity at various spin coating speeds is compared, revealing that a rotation speed of 1000 r.p.m. yields a higher absorption intensity across the

300–2500 nm range compared to other TiN/Ag films and the bare Ag film. Subsequently, a 50 nm thick layer of CaF₂, with a refractive index of 1.434 (intermediate between that of TiN (≈1.5–2.2) and free space) was evaporated onto the TiN layer, resulting in enhanced absorption in the near-infrared region. The final structure of the broadband absorber is composed of CaF₂ (50 nm)/TiN NPs (1000 r.p.m.)/Ag (100 nm). Figure S21c (Supporting Information) shows the uniformly black optical image of the broad-spectrum absorber. Figure S21d's (Supporting Information) top-view SEM image confirms that a uniform TiN film is easily prepared via spin-coating. The cross-sectional SEM image in Figure S21e (Supporting Information) reveals a TiN NPs layer thickness of ≈5.8 μm. Figure S21f (Supporting Information) illustrates the temperature changes of the absorber under laser irradiation at various wavelengths with a constant power of 6 mW. The minimal variations in temperature increase among different wavelengths demonstrate the absorber's high photothermal conversion efficiency across a broad spectrum. Figure S22 (Supporting Information) displays thermal images of the absorber under laser illumination at different wavelengths. The pre-prepared broadband absorber was then dry-transferred onto the Ag⁺-doped side of the MHP SCs for device fabrication. Figure 3a shows a schematic of a lateral broadband PD utilizing the PTEE. The counter electrodes consist of a stratified architecture, incorporating the previously described broadband absorber atop the Ag electrodes. The PTEE material is an n-type MHP layer doped with Ag⁺. Upon exposure of one end of the broadband absorption electrode to laser illumination within the wavelength range of 360 to 2200 nm, localized heating occurs, establishing a thermal gradient with a hot end and a cooler, unexposed end. This temperature differential induces a carrier concentration gradient across the counter electrodes, thereby generating a photogenerated thermoelectric voltage. The measured electrical voltage (ΔU) can be represented by the equation $\Delta V = -S\Delta T$, where S denotes the Seebeck coefficient and ΔT represents the temperature difference. Consequently, the thermoelectric voltage response of our lateral PD is influenced by both the Seebeck coefficient and the temperature difference between the counter electrodes. Initially, we evaluated the performance of lateral PDs incorporating an Ag⁺ doped layer in comparison to those based on intrinsic MHP SC. As illustrated in Figure S23 (Supporting Information), the lateral PD with an Ag⁺ doped layer exhibited 1.4 times of magnitude enhancement in photovoltage response to a 2200 nm laser, relative to the undoped condition, demonstrating that the Seebeck coefficient was significantly improved by Ag doping. Introducing a vertical electric field in a p-n junction directs photogenerated carriers, reducing carrier recombination and Seebeck voltage losses in PTE devices.^[41] Figure 3b,c present a summary of the voltage response and the calculated R_V of the lateral broadband PD, which operates across a spectral range from ultraviolet (360 nm) to near-infrared (2200 nm) at a power level of 6 mW. Owing to the PTEE, the PD demonstrates broadband photodetection capabilities. The maximum R_V recorded is 10 V W⁻¹ under 532 nm laser illumination. While for 2200 nm, the R_V decreases to 0.6 V W⁻¹. Subsequently, I - V characteristics were measured both with and without laser illumination, as depicted in Figure 3d. The illuminated I - V curves exhibit a downward shift compared to the dark Ione, with no significant alteration in the extracted resistance. These phenomena are characteristic

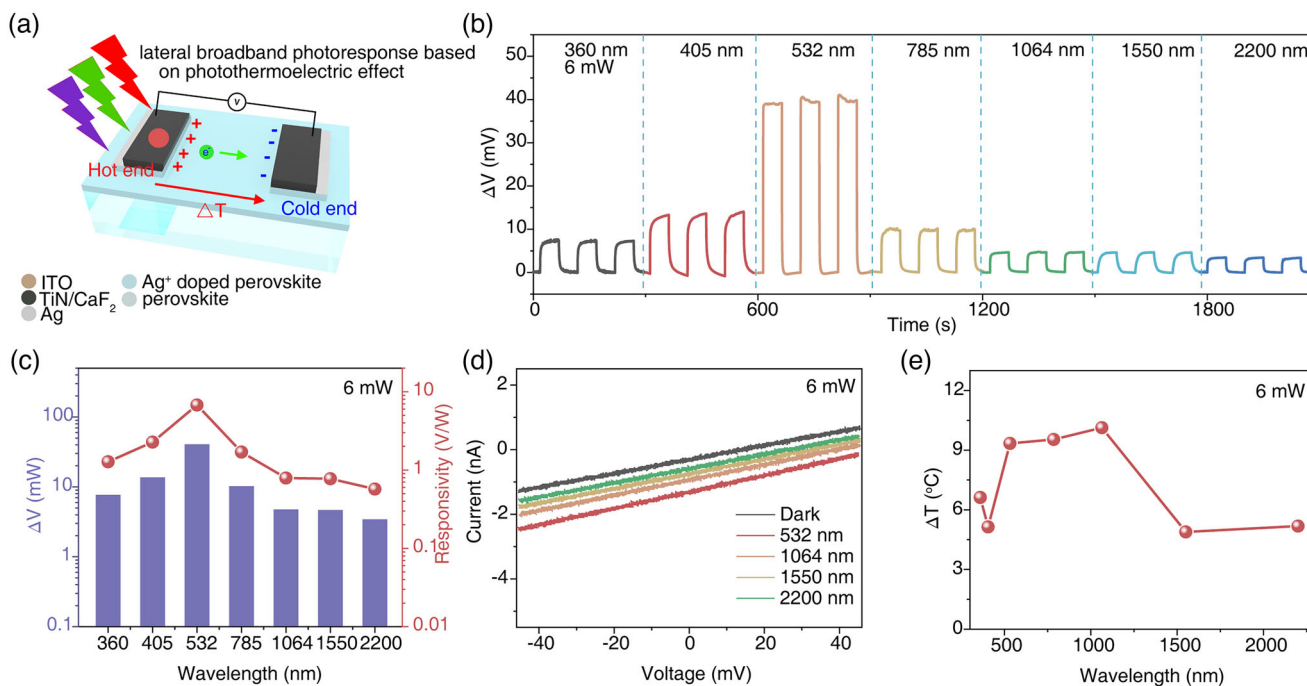


Figure 3. Performances and working mechanism of the lateral broadband PD-based on MAPbBr₃: Ag⁺ SC surface. a) Schematic diagram of lateral broadband PD-based on lateral PTE. b) The PTE voltage response of lateral broadband PD under 360–2200 nm laser illumination with a power of 6 mW. c) Laser wavelength-dependent PTE voltage (left) and corresponding responsivities (right) of the lateral broadband PD. d) *I-V* characteristics of the lateral PD under dark, 532, 1064, 1550, and 2200 nm laser illumination with a power of 6 mW. e) The temperature difference between two counter electrodes under 360–2200 nm laser with a power of 6 mW.

of the PTEE. The downward movement trend aligns with the photovoltage in Figure 3b. Figure 3e displays the temperature difference of the counter electrodes when a broadband absorption electrode is laser-irradiated at various wavelengths (6 mW). Figure S24 (Supporting Information) provides the corresponding thermal images. The temperature difference trends closely match the wavelength-dependent photoresponse voltage, further confirming that the photoresponses stem from the PTEE. The calculated Seebeck coefficient was $\approx 780 \text{ V K}^{-1}$.

The photoresponses in the long-wavelength NIR region were demonstrated. Figure 4a compares the time-dependent temperature difference (ΔT) and voltage (ΔV) between two electrodes at different power levels at 2200 nm, showing similar growth trends. Figure 4b highlights the strong linear relationship between ΔV and laser power at 2200 nm, confirming the PTEE, with a R_V of 0.493 V W^{-1} . Under 2200 nm laser illumination, the broadband PD exhibits a rise time of 3.07 s and a fall time of 4.53 s (Figure S25b, Supporting Information). Figure S26 (Supporting Information) presents the thermal imaging results depicting the temperature differential of the electrode within the device when exposed to 2200 nm laser illumination. The observed change in temperature difference exhibits a certain linear correlation with the laser power. A comparative analysis with previously reported perovskite broadband PDs (Table 1) demonstrates that our PDs exhibit a notably wide spectral response range. Furthermore, the self-powered capability and dual-modal ability of our devices represents a significant advantage, as many existing perovskite broadband PDs require external power sources for operation. As illustrated in Figure

S27a (Supporting Information), the voltage demonstrates a sensitive response to the periodic activation and deactivation of the light source at varying power levels of the 532 nm laser. This is attributed to the absorption of the 532 nm laser by MAPbBr₃, facilitated by light scattering. Consequently, the PD's voltage response under 532 nm laser illumination is a combination of the thermoelectric voltage and the photovoltage. Consequently, no linear correlation exists between the voltage response and the incident power (Figure S27b, Supporting Information). In contrast, a strong linear relationship is observed between the photoinduced temperature change of the counter electrodes and the 532 nm laser power (Figure S27d, Supporting Information). The rise and fall times of the broadband PD at 532 nm are measured to be 255 ms and 323 ms, respectively (Figure S27e, Supporting Information). Additionally, we assessed the temperature and voltage photoresponses of the lateral PD when exposed to 1064 nm and 1550 nm lasers (Figures S29–S32, Supporting Information). Similarly, the temperature variation and voltage responses exhibit robust linear correlations with increasing laser power, akin to the conditions observed at 2200 nm. The rise and fall times of the broadband PD under a 1064 nm laser have been determined to be 4.57 s and 11.65 s, respectively. In contrast, for a 1550 nm laser, the rise and fall times are measured to be 12.48 s and 13.65 s, respectively. Furthermore, the strategy of Ag⁺ doping, in conjunction with a broadband absorber, proves to be effective for other MHP SCs. We then fabricated lateral PDs using MAPbCl₃: Ag⁺ and MAPbI₃: Ag⁺ PDs as thermoelectric layers and examined their photoresponses. Figure S33a,b (Supporting Information) summarize the voltage

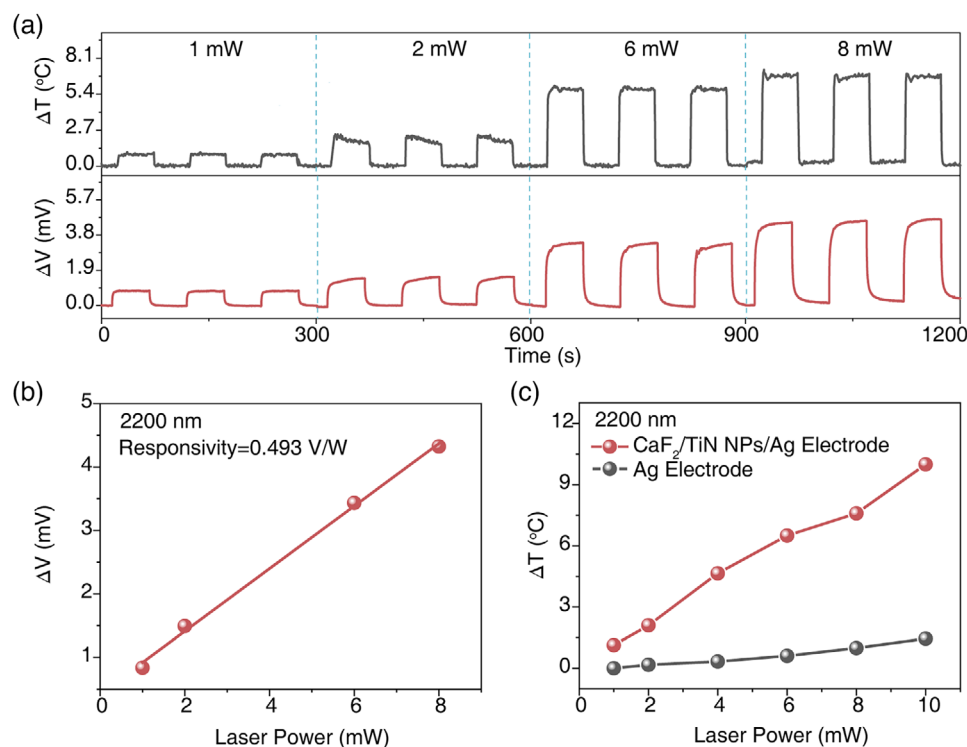


Figure 4. a) The temperature change (up) and voltage change (down) of the lateral broadband PD-based on MAPbBr₃: Ag⁺ SC surface under 2200 nm laser illumination with different powers. b) Thermoelectric photovoltage as a function of 2200 nm laser power. The red line is the linear fit to the data, with an obtained R_V of 0.493 V W⁻¹. c) The comparison of temperature difference between the two kinds of counter electrodes with the increase of the 2200 nm laser power.

response and R_V of MAPbCl₃-based PD under lasers from ultraviolet (360 nm) to near-infrared (2200 nm) wavelengths, showing excellent broadband photodetection performance. Figure S33c,d (Supporting Information) show the MAPbCl₃: Ag⁺-based lateral PD's voltage response to a 2200 nm laser, revealing a linear relationship with power and a R_V of 0.38 V W⁻¹. Figure S34a,b (Supporting Information) summarize the MAPbI₃: Ag⁺-based lateral PD's voltage response and R_V , effective from 360 to 2200 nm, demonstrating broadband photodetection ability. Furthermore, Figure S34c,d (Supporting Information) depict the voltage response of the MAPbI₃-PD toward 2200 nm lasers at varying power levels. It is noteworthy

that the voltage response demonstrates a robust linear correlation with the laser power, achieving a R_V of 0.91 V W⁻¹. Both two PDs demonstrate obvious broadband photodetection behaviors, with the highest responses occurring for light with wavelength close band gap (405 and 785 nm, respectively). These reproducible broadband photodetection performances indicate that our strategy is universally applicable to MHPs with different band gaps. The lateral broadband PD exhibits an effective full-spectrum response, while the vertical narrowband PD is capable of detecting specific wavelengths. By integrating narrowband and broadband dual-modal photodetection within a single device, it is possible to achieve double-encrypted information

Table 1. Comparison of response range of broadband or infrared photodetector based on metal halide perovskite.

Device structure	Spectral range	Responsivity	Bias [V]	Ref.
Ag/PCBM/ MAPbI ₃ /Pedot: PSS/ITO	300-800 nm	329 mA W ⁻¹	0	[7]
Au/MAPbCl ₃ /Bi-MAPbBr ₃ /Bi-MAPbI _{2.5} Br _{0.5} /MAPbI ₃ /Au	828 nm	18 mA W ⁻¹	40	[8]
ITO/MAPbI ₃ /Si/Ag	360-1550 nm	4 mA W ⁻¹ @ 780 nm	0	[16]
Au/MAPbI _{3-x} Br _x /n-MAPbBr ₃ /MAPbI ₃ /Au	400-830 nm	0.21 A W ⁻¹ @ 820 nm	-3	[21]
Ag/2D perovskite layer/MAPbI ₃ /Ag	0.1 THz	88.8 μA W ⁻¹ @ 0.1 THz	6	[22]
Carbon/MAPbI ₃ /Carbon	980-2200 nm	0.21 V W ⁻¹ @ 2200 nm	0	[23]
ITO/MAPbCl ₃ (Single crystal film)/PTAA/Au	1.55-4 μm	4.3 mA W ⁻¹ @ 1550 nm	2.5	[24]
Perovskite/Te	X-ray-1550 nm	0.34 A W ⁻¹ @ 1550 nm	5	[42]
CaF ₂ /TiN/AgMAPbBr ₃ : Ag ⁺ /MAPbBr ₃ /Ag	360-2200 nm	0.493 V W ⁻¹ @ 2200 nm	0	This work

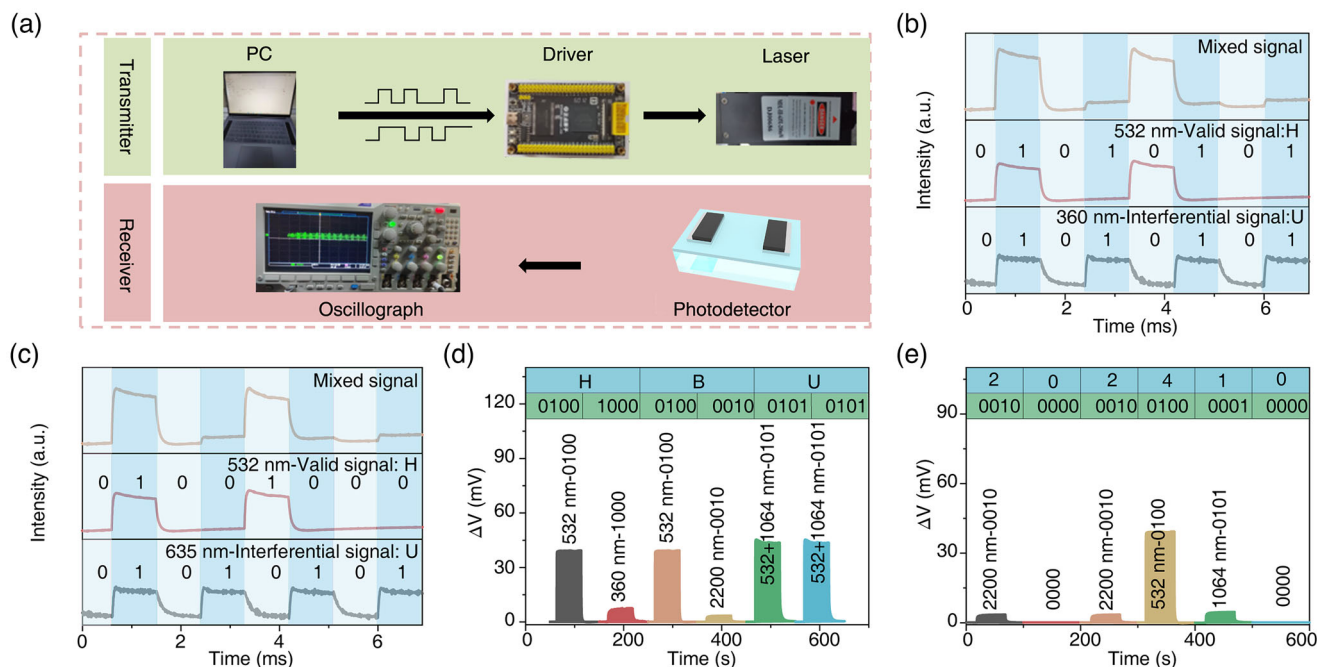


Figure 5. a) Schematic diagram of the SOC system with transmitter and receiver subsystems. b) The mixed signal generated by 532 and 360 nm mixed laser illumination on a vertical narrowband MAPbBr₃-based PD. c) The mixed signal generated by 532 and 635 nm mixed laser illumination on a vertical narrowband MAPbBr₃-based PD. d) 24-bit ciphertext “HBU” and e) 24-bit key “202 410” using the lateral broadband MAPbBr₃-based PD.

transmission. Furthermore, by altering the type of halide, the specific wavelength of the PDs can be adjusted from blue-violet to red light, thereby expanding its range of applications.

Subsequently, we incorporated the MAPbBr₃-based dual-modal PD as an optical signal receiver within a secured optical communication (SOC) system, as depicted in Figure 5. As shown in Figure 5a, the system consists of an emitter component, which is responsible for driving the laser, and a receiver component, which is tasked with signal processing. In this setup, digital data from the computer is transmitted through the modulation of two lasers, operating at wavelengths of either 360 nm and 532 nm, or 532 nm and 635 nm. The combined signal is then detected by the PD and displayed on the oscilloscope. For the vertical narrowband PD-based on MAPbBr₃, the device is capable of transmitting information carried specifically by a 532 nm laser, while demonstrating reduced interference from 360 and 635 nm lasers (Figure 5b,c). This suggests that the narrowband PD is relatively unaffected by ambient light during optical communication transmission. Owing to the rapid response speed of the PDs, variations in coding frequency do not impact the encoding process. As illustrated in Figure S35 (Supporting Information), the device successfully receives modulated optical information at various bit rates, demonstrating the system’s capability to transmit data at these rates up to 4.8 kbps. While the lateral broadband PDs exhibit a wide spectral response from ultraviolet light to infrared light at zero bias. Then, the prepared broadband PD-based on MAPbBr₃ SC is integrated into the SOC system as an optical signal receiver. The encoded information, converted into the American Standard Information Exchange Code (ASCII), can be transmitted utilizing a four-color light as

a carrier in conjunction with an encryption protocol. When the four-color lights with wavelengths of 360, 532, 1064, and 2200 nm are simultaneously activated, the PD produces a binary output representing the voltage information in the “1111” state. Conversely, when all four-color lights are deactivated simultaneously, the device outputs a binary representation of the current information in the “0000” state. By manipulating the switching mechanism of a four-color light system, the device is capable of producing 16 distinct four-bit binary states, each corresponding to unique coding information. To enhance the security of information transmission, the key “202 410” is applied to the transmitted letters “HBU” (as illustrated in Figure 5c). Here, the binary sequences “0 100 1000”, “0 100 0010”, and “0 101 0101” represent the letters “H”, “B”, and “U”, respectively. Additionally, the binary sequences “0010”, “0000”, “0010”, “0100”, “0010”, “0000”, “0010”, and “0100” correspond to the digits “2”, “0”, “2”, “4”, “1”, and “0”, respectively (Figure 5d,e; Figure S36, Supporting Information). The process of combining the key with the encrypted message involves interspersing the four-bit binary encoding of the key within the two sets of four-bit binary encodings of the message. For instance, consider the signal “H”, which is initially encoded as “0 100 1000”. The key, represented by the four-bit binary codes “2 (0010)” and “0 (0000)” are inserted into the message encoding at specific intervals, resulting in the combined signal “010 000 101 000 0000”. PDs with UV–Vis–NIR broadband photoresponse can easily detect this encoded light signal, accurately matching the original encrypted data. The above results with high accuracy and security for information transmission confirm that our dual-modal PDs have strong potential in encrypted optical communication.

3. Conclusions

In summary, we have successfully demonstrated MAPbX₃: Ag⁺ SCs-based dual-modal PDs operating in both broadband and narrowband regimes. Due to the CCN-assisted IPPE formed at the vertical p-n junction, self-powered and high-performance narrowband PDs-based on MAPbBr₃ exhibit a narrow FWHM of ≈113 nm, a R_i of 0.36 A W⁻¹, a fast rise time of 77 μs, and a fall time of 157 μs. Then, when further employing TiN-based broadband absorber onto the lateral PD-based on PTEE, a broadband PD with a high broad spectral response (from 360–2200 nm), a high R_v of 0.6 V W⁻¹ (2200 nm) without an external bias was realized. By changing the halide type of the MHP SCs, the specific response band of narrowband PD can be modulated from purple light to red light, while maintaining the wide spectrum response capability. By utilizing the narrowband and broadband photoreponses in a single device, we successfully achieved double encryption in signal transmission. This work introduces a new approach for self-powered dual-modal devices and highlights their dual-function application, marking significant progress toward high-performance, multifunctional perovskite-based integrated devices. Compared with the existing optical encryption technology, our communication encryption method does not require high-precision optical components and equipment, and the cost is lower. It can also be well compatible with electronic information systems, integrated with computer and network systems, and widely used in practice.

Supporting Information

Supporting Information is available from the Wiley Online Library or from the author.

Acknowledgements

This work was supported by the National Natural Science Foundation of China (Grant Nos. 62104057, 52125205, 52472158), Hebei Education Department (Grant No. BJK2022050), the Science and Technology Plan Project of Hebei Province (Grant No. 226Z1002G), the Research Innovation Team Project of Hebei University (IT2023A04), Hebei Province Optoelectronic Information Materials Laboratory Performance Subsidy Fund Project (No. 22567634H), Interdisciplinary Research Program of Natural Science of Hebei University (DXK202304, DXK202212).

Conflict of Interest

The authors declare no conflict of interest.

Data Availability Statement

The data that support the findings of this study are available from the corresponding author upon reasonable request.

Keywords

dual-modal photodetector, interfacial pyro-phototronic effect, perovskite single crystal, photothermoelectric effect, secured optical communication

Received: November 21, 2024

Revised: January 21, 2025

Published online:

- [1] H. Dan, H. Li, L. Xu, C. Guo, C. R. Bowen, Y. Yang, *Infomat* **2024**, *6*, 12531.
- [2] J. Xiong, Q. Yu, X. Hou, B. Liu, S. Li, H. Deng, Z. Yang, J. Leng, S. Zhu, Y. Sun, Z. Jiang, N. Huo, J. Wu, P. Zhou, *Adv. Funct. Mater.* **2024**, *34*, 2314972.
- [3] L. Min, H. Sun, L. Guo, M. Wang, F. Cao, J. Zhong, L. Li, *Nat. Commun.* **2024**, *15*, 2066.
- [4] Y. Shi, X. Li, G. Chen, M. Zou, H. Cai, Y. Yu, X. Zhang, *Nat Photon* **2024**, *18*, 610.
- [5] S. Liu, S. Jiao, Y. Zhao, H. Lu, S. Yang, D. Wang, S. Gao, J. Wang, L. Zhao, *Adv. Opt. Mater.* **2023**, *11*, 2300831.
- [6] T. Yan, Z. Li, L. Su, L. Wu, X. Fang, *Adv. Funct. Mater.* **2023**, *33*, 2302746.
- [7] W. Cheng, W. Tian, F. Cao, L. Li, *Infomat* **2022**, *4*, 12348.
- [8] Y. Pan, X. Wang, D. Zhang, Z. Wei, Y. Xu, Y. Li, Q. Li, Z. Zhao, Z. Zhu, B. S. Bae, D. C. Onwudiwe, X. Xu, W. Lei, *ACS Photon.* **2024**, *11*, 1252.
- [9] B. Huang, J. Liu, Z. Han, Y. Gu, D. Yu, X. Xu, Y. Zou, *ACS Appl. Mater. Interfaces* **2020**, *12*, 48765.
- [10] L. Guo, H. Wang, Z. Xu, R. Cong, L. Zhao, S. Zhang, K. Zhang, L. Gao, S. Wang, C. Pan, Z. Yang, *Adv. Funct. Mater.* **2023**, *33*, 2306526.
- [11] L. Guo, X. Yang, Y. Liang, Z. Wu, X. San, Z. Wang, L. Li, Z. Liu, J. Chen, S. Wang, X. Zhang, C. Pan, Z. Yang, *Nano Lett.* **2024**, *24*, 11599.
- [12] Z. Li, T. Yan, X. Fang, *Nat. Rev. Mater.* **2023**, *8*, 587.
- [13] L. Guo, X. Liu, L. Gao, X. Wang, L. Zhao, W. Zhang, S. Wang, C. Pan, Z. Yang, *ACS Nano.* **2022**, *16*, 1280.
- [14] T. Yan, Z. Li, L. Su, L. Wu, X. Fang, *Adv. Function. Mater.* **2023**, *33*, 2302746.
- [15] P. Vashishtha, I. H. Abidi, S. P. Giridhar, A. K. Verma, P. Prajapat, A. Bhoriya, B. J. Murdoch, J. O. Tollerud, C. Xu, J. A. Davis, G. Gupta, S. Walia, *ACS Appl. Mater. Interfaces* **2024**, *16*, 31294.
- [16] Z. Yang, H. Wang, L. Guo, Q. Zhou, Y. Gu, F. Li, S. Qiao, C. Pan, S. Wang, *Small* **2021**, *17*, 2101572.
- [17] Y. Pan, X. Wang, Y. Liao, Y. Xu, Y. Li, Q. Li, X. Zhang, J. Chen, Z. Zhu, Z. Zhao, E. E. Elemike, M. Furuta, W. Lei, *ACS Appl. Mater. Interfaces* **2022**, *14*, 50331.
- [18] D. Zhang, Y. Pan, X. Wang, Z. Wei, Y. Xu, D. C. Onwudiwe, B. S. Bae, M. Ertugrul, J. Zhou, X. Xu, W. Lei, *J. Mater. Chem. C* **2024**, *12*, 12806.
- [19] A. Perveen, Y. Xu, S. M. Abubakar, P. Sellan, W. Xin, F. Saeed, S. Hussain, B. S. Bae, J. Zhou, Y. Zhu, W. Lei, *Adv. Opt. Mater.* **2024**, *12*, 2302918.
- [20] T. Chen, Z. Liu, L. Zhang, H. Wu, G. Wu, H. Chen, *ACS Appl. Mater. Interfaces* **2023**, *15*, 50312.
- [21] J. Zhao, X. Wang, Y. Xu, Y. Pan, Y. Li, J. Chen, Q. Li, X. Zhang, Z. Zhu, Z. Zhao, E. E. Elemike, D. C. Onwudiwe, B. S. Bae, S. Bin Sha, W. Lei, *ACS Appl. Mater. Interfaces* **2022**, *14*, 25824.
- [22] J. Li, Y. Zou, D. Hu, Y. Gu, Z. Han, J. Liu, X. Xu, *Nanoscale* **2022**, *14*, 6109.
- [23] Y. Xiong, Z. Shen, S. Yuan, Y. Liu, T. Jin, Y. Liang, R. Masrour, G. Niu, L. Xu, *Chem. Eng. J.* **2023**, *477*, 147168.
- [24] S. Liu, Y. Ding, W. Rong, Y. Xu, Y. Li, D. C. Onwudiwe, B. S. Bae, M. Ertugrul, Y. Zhu, Z. Wu, W. Lei, Q. Li, X. Xu, *ACS Nano.* **2024**, *18*, 25226.
- [25] S. Hu, Z. Ren, A. B. Djurišić, A. L. Rogach, *ACS Energy Lett.* **2021**, *6*, 3882.
- [26] Y. Zhou, J. Wang, D. Luo, D. Hu, Y. Min, Q. Xue, *Nano Energy* **2022**, *94*, 106949.
- [27] C. Li, X. Chen, N. Li, J. Liu, B. Yuan, Y. Li, M. Wang, F. Xu, Y. Wu, B. Cao, *J. Mater. Chem. C* **2020**, *8*, 3694.
- [28] W. Tang, J. Zhang, S. Ratnasingham, F. Liscio, K. Chen, T. Liu, K. Wan, E. S. Galindez, E. Bilotti, M. Reece, M. Baxendale, S. Milita, M. A. McLachlan, L. Su, O. Fenwick, *J. Mater. Chem. A* **2020**, *8*, 13594.

- [29] M. A. Haque, S. Kee, D. R. Villalva, W. L. Ong, D. Baran, *Adv. Sci.* **2020**, *7*, 1903389.
- [30] T. Schramm, M. Deconinck, R. Ji, E. Siliavka, Y. J. Hofstetter, M. Löffler, V. V. Shilovskikh, J. Brunner, Y. Li, S. Bitton, N. Tessler, Y. Vaynzof, *Adv. Mater.* **2024**, *36*, 2314289.
- [31] Y. J. Fang, Q. F. Dong, Y. C. Shao, Y. B. Yuan, J. S. Huang, *Nat. Photon.* **2015**, *9*, 679.
- [32] Y. Liu, Y. Zhang, Z. Yang, D. Yang, X. Ren, L. Pang, S. Liu, *Adv. Mater.* **2016**, *28*, 9204.
- [33] X. Guo, N. Li, Y. Xu, J. Zhao, F. Cui, Y. Chen, X. Du, Q. Song, G. Zhang, X. Cheng, X. Tao, Z. Chen, *Adv. Funct. Mater.* **2023**, *33*, 2213995.
- [34] L. Guo, Y. Song, B. Wang, R. Cong, L. Zhao, S. Zhang, L. Li, W. Wu, S. Wang, X. San, C. Pan, Z. Yang, *ACS Appl. Mater. Interfaces* **2024**, *16*, 16482.
- [35] X. Chen, P. V. Kamat, C. Janáky, G. F. Samu, *ACS Energy Lett.* **2024**, *9*, 3187.
- [36] P. P. Joshi, S. F. Maehrlein, X. Zhu, *Adv. Mater.* **2019**, *31*, 1803054.
- [37] J. Fu, S. Ramesh, J. W. Melvin Lim, T. C. Sum, *Chem Rev.* **2023**, *123*, 8154.
- [38] Y. S. Yuze Lin, J. Dai, T. Li, Ye Liu, X. Dai, X. Xiao, Y. Deng, A. Gruverman, X. C. Zeng, J. Huang, *Nat Commun.* **2021**, *12*, 7.
- [39] M. M. Yang, Z. D. Luo, Z. Mi, J. Zhao, P. E. S., M. Alexe, *Nature* **2020**, *584*, 377.
- [40] Y. Li, C. Lin, K. Li, C. Chi, B. Huang, *Nano Lett.* **2022**, *22*, 5659.
- [41] R. Chen, L. Chen, Z. Liang, *ACS Energy Lett.* **2024**, *9*, 5721.
- [42] Y. C. He, G. H. Dun, J. Deng, J. L. Peng, K. Qin, J. H. Zhang, X. S. Geng, M. S. Zhang, Z. S. Wang, Y. Xie, Z. Q. Bai, D. Xie, H. Tian, Y. Yang, T. L. Ren, *Adv. Sci.* **2025**, 2414259.